WILEY | Hindawi

Research Article

Flow in Microchannels between Sealing Surfaces of Casing Connections: LBM Simulation

Feng Ye [iD],[1] **Feng Chen** [iD],[2] **Wenchang Wang** [iD],[1] **Renliang Zhang**,[3] **Xing Zhou**,[1] **Ken Qin**,[1] **and Qinfeng Di** [iD][1]

[1]*Shanghai Institute of Applied Mathematics and Mechanics, School of Mechanics and Engineering Science, Shanghai University, Shanghai 200444, China*
[2]*School of Mechatronics Engineering and Automation, Shanghai University, Shanghai 200444, China*
[3]*Key Laboratory of Mechanical Reliability for Heavy Equipment and Large Structures of Hebei Province, School of Civil Engineering and Mechanics, Yanshan University, Qinhuangdao 066004, China*

Correspondence should be addressed to Feng Chen; chenfeng536@126.com, Wenchang Wang; wangwenchang1982@163.com, and Qinfeng Di; qinfengd@sina.com

Great difficulties have been encountered in the study of the seal failure of casing connection. The in situ microscopic seal surfaces under complex loads are hard to be obtained due to the engagement characteristics of thread. In this study, a method to construct the microscopic seal surfaces of a specified $7''$ casing PTC under complex loads was proposed. Then, the lattice Boltzmann method (LBM) was applied to simulate the fluid flow inside the microchannel between the seal surfaces. The effect of pressure gradient and wettability on the flow behavior of a multicomponent fluid system at the microscopic scale was analyzed. Pressure gradient has a huge influence on the volume fraction of sealing compound and the average velocity of displacing fluid. The volume fraction of sealing compound decreases with the increase of pressure gradient. Break-through can be observed for fluid systems with relatively larger pressure gradient. For the systems with $\Delta p = 0.658$, $\Delta p = 0.439$, and $\Delta p = 0.219$, the break-through time steps are around 61000, 99000, and 295000, respectively. Wettability has huge impact on the distribution of sealing compound, and break-through was not observed for the fixed pressure difference $\Delta p = 0.110$ with various wettability. It is expected to provide some new insights for understanding the seal failure of casing connections at the microscopic level.

1. Introduction

A notable growth in the proportion of deep and ultradeep wells over the world has been observed in recent years. As the well depth increases, the service environment of oil and gas tubular strings becomes more severe. Tubular strings may not only bear huge axial tension, large bending moment, and high external pressure but also may face the challenges brought by high temperature (150°C~300°C), high pressure (up to 241 MPa), harsh geological conditions, and corrosive environments. The integrity of tabular strings will be seriously damaged when facing such severe conditions. According to statistics, annular pressure exists in more than 50% of the ultradeep gas wells in key blocks of TLM oil and gas field, and one of the main causes responsible for that issue is the seal failure of tubular strings [1].

The integrity of tubular strings has been studied by many scholars from the aspects of crustal stress, formation creep, fault dislocation, corrosion environment, hydraulic fracturing conditions, and cement ring seal failure [2–7]. Most of them consider the string as a whole; less attention was paid to threaded connections. However, statistics show that about 90% of the integrity failures relate to the seal failure of threaded connections in gas wells [8]. Moreover, this kind of seal failure also occurs in recognized high-quality premium threaded connections (PTC), whose sealing performance has been rigorously validated in the laboratory. Focusing on the seal failure of threaded connections, several

researches have been carried out. Schwind discussed various factors that affect the sealing performance of API round threaded connections, and the equations for stress and leak resistance were proposed based on the elastic theory [9]. Gong studied the effect of the tolerance of thread height, thread angle, and thread taper on the sealing performance of standard API casing threaded connections [10]. Xu et al. proposed an analytical method to discuss the influence of the wall thickness and the taper of seal surface on the sealing performance of non-API casing threaded connections [11]. Based on the Hertz equation and sealing contact energy, Xu et al. established an analytical model for calculating the gas tight seal pressure of PTCs and studied the effect of spherical radius, cone and taper, and the applied torque of the seal surface on the gas tight sealing performance of connections [12]. It should be pointed out that the above analyses based on the classical elastic theory are surely incapable of describing the elastoplastic deformation of threaded connections under complex loads.

However, under complex loads, the elastoplastic deformation of threaded connections is one of the highly concerned factors. Except for the analytical methods, some researchers turn to methods combining experiments and numerical analyses. Mimaki et al. pointed out that the contact pressure of gas tight seal was 5.6 to 6.0 times that of water tight seal through 2D finite element analyses (FEA) and physical testing [13]. Ogasawara et al. studied the sealing performance of metal-to-metal sealing structures [14]. It is found that the critical leaking pressure relies on both the average contact pressure and the contact area. Marie et al. studied the metal-to-metal seal under the make-up torque and developed a test equipment and a calculating method for measuring the fluid leakage rate [15]. Other variables such as seal material properties, use or not of sealing compound, and surface topography also affect the seal performance. Murtagian et al. studied the influence of contact pressure and length, load history, and the use of sealing compounds on the effectiveness of stationary metal-to-metal seals [16]. A criterion containing a sealability parameter and a critical value obtained from experiments was proposed. The leakage threshold following the proposed criterion is more conservative than ISO 13679. Xie et al. modified this criterion and proposed that the seal contact strength (the integral of the sealing pressure with respect to the effective seal length) of 250 N/mm is the acceptable leakage threshold for high temperature wells [17, 18]. Wang et al. studied the distribution of contact pressure and contact length of two sealing structures, e.g., cone-cone and sphere-cone, with 2D FEA, and obtained the variation characteristics of sealing performance for the two sealing structures [19].

It is worth mentioning that the results obtained by 2D FEA are incapable of accurately reflecting the contact state of the seal surfaces since the helix angle of thread has been ignored. Few studies have successfully implemented 3D FEA of threaded connections in ANSYS and ABAQUS [20–24]. The necessity of applying 3D FEA instead of 2D FEA has been demonstrated in these studies. Since the helix angle of thread is ignored in 2D FEA, the contact state of the seal surfaces cannot be accurately reflected. Under complex loads, the deformation of the seal surfaces of threaded connection is quite complicated as well as the estimation of the contact behavior of the seal surfaces. For a long period of time, most researchers suppose that as long as the average contact pressure on the metal-to-metal seal surface of threaded connection surpasses the fluid pressure inside the pipe to be sealed, leakage will hardly be observed. Unfortunately, in practice, leakage still occurs for metal-to-metal sealing structures designed following the above perception. It is quite reasonable to assume that the existence of advantage channel at the microscopic scale is responsible for those leakages, since existing processing methods inevitably lead to surface roughness. Therefore, the flow behavior inside the microchannels between the seal surfaces is of great importance to understand the seal failure of casing connection.

The lattice Boltzmann method (LBM) is a method for computational fluid dynamics based on the mesoscopic kinetic theory [25, 26], with several well-known features such as high computational efficiency, easiness of handling complex geometric boundaries [27], and natural parallelism in algorithm. The LBM has been widely used for simulating flow problems of multiphase or multicomponent fluid at the microscopic scale [28–30]. Xu et al. proposed a theoretical method of leakage prediction for compressive seals in planer solid oxide fuel cells (pSOFCs) and pointed out that LBM simulations of the flow in three-dimensional (3D) rough interfacial gaps are rarely reported [31]. In this study, the LBM was applied to simulate the fluid flow inside the microchannel between the seal surfaces of a specified $7''$ casing PTC under certain complex loads. The effect of pressure gradient and wettability on the flow behavior of a multicomponent fluid system at the microscopic scale was analyzed. It is expected to provide some new insights for studying the seal failure of casing connections.

2. Microchannels between the Seal Surfaces of Casing Connection

2.1. Three-Dimensional Elastoplastic FEA of PTCs. The $7''$ casing PTC containing a metal-to-metal sphere-cone sealing structure is shown in Figure 1, and its main geometric parameters are listed in Table 1. The buttress thread form of the casing connection can be found in the API standard [32], and the tolerance of the thread is omitted. The mesh of the elastoplastic finite element model is shown in Figure 1 as well, with the element type being C3D8I. Distributing coupling elements are constructed on the pin-free end to apply external loads, while the kinematic coupling elements are constructed on the box free end to impose constraints. Contact surfaces are defined on the threads and shoulders to simulate the interaction between the pin and box. Detailed information about the modeling techniques can be found in Ref. [20]. The total numbers of nodes and elements are 6.045 million and 4.955 million, respectively. The loading condition analyzed in the current work is derived from a real service environment. It is a combination of make-up torque (22.6 kN·m), axial tension (670.0 kN),
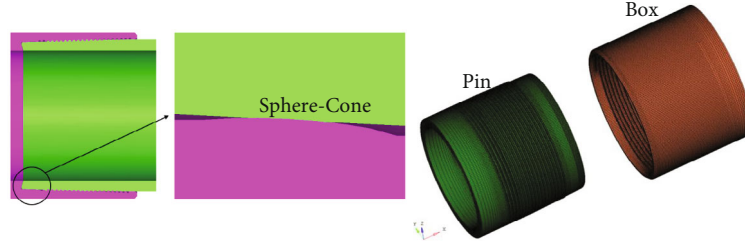
FIGURE 1: Sealing structure and 3D finite element model of the $7''$ casing PTC.

TABLE 1: Geometric parameters of the $7''$ casing PTC.

Thread pitch	5.08 mm (1/5$''$)
Thread taper	1 : 16
Thread shape	Buttress
Outer diameter of the coupling	194.5 mm
Inner diameter of the pipe	152.5 mm
Outer diameter of the pipe	177.8 mm ($7''$)
Sealing type	Sphere-cone
Cone taper	1 : 16
Reverse shoulder	-15°
Shoulder clearance	0.2 mm
Radius of the sphere	15 mm

TABLE 2: Relationship between true stress and plastic strain.

True stress/ MPa	Plastic strain	True stress/ MPa	Plastic strain	True stress/ MPa	Plastic strain
734.9	0	932.2	0.0315	990.0	0.0677
764.3	0.0001	945.8	0.0379	994.7	0.0730
869.0	0.0057	957.5	0.0440	998.4	0.0780
885.7	0.0122	967.9	0.0503	1000.3	0.0830
901.3	0.0186	976.5	0.0562	1010.3	0.0831
917.7	0.0252	983.9	0.0620	—	—

bending (27.5 kN·m), internal pressure (120 MPa), and external pressure (80 MPa). The material of threaded connections is an isotropic elastic-plastic material. Its Young's modulus and Poisson's ratio are 210 GPa and 0.29, respectively. The true stress-plastic strain data of material given by the tensile test is shown in Table 2.

The obtained distributions of von Mises stress and strain are shown in Figure 2. Relatively high levels of von Mises stress are observed on the seal surface and the thread teeth at both ends. The maximum value reaches 875.8 MPa while the material yield limit of P110 casings is around 758.5 MPa, indicating that the seal surfaces have been subjected to certain plastic deformation under the above loading condition.

It is assumed that advantage channel with small leakage resistance at the microscopic level is responsible for fluid leakage. Hence, the minimum contact pressure on the seal surface determines the sealing performance. The distribu-tion of contact pressure on the seal surface is shown in Figure 3. It is found that the contact pressure on the seal surface distributed unevenly along the axial direction due to the thread taper while it is relatively uniform along the circumferential direction. The nonuniformity along the circumferential direction is mainly caused by the asymmetric characteristics of the end of thread and asymmetric load such as bending moment. The contact pressure is relatively high near the vertex of the spherical zone and gradually decreases along the axial direction. The maximum contact pressure on the seal surface reaches 1394.2 MPa. Noticing that a circumferential path, an axial path, and a point were labeled as "a," "b," and "o" separately in Figure 3, the circumferential path "a" connects all the points with maximum contact pressure along the axial direction, and "o" is the point with the lowest value in this line. The axial path "b" goes through point "o" and is considered as the dominant path with relatively low leakage resistance.

Based on the theory of seal contact energy [33], the average contact pressure on the axial path "b" can be derived as

$$P_{ca} = \frac{f_s}{L_s}, f_s = \int_0^{L_s} P_c(x) dx, \tag{1}$$

where L_s is the contact width and f_s is the seal contact strength.

The contact pressure along the axial path "b" can be estimated with the polynomial fitting

$$P_c(x) = -85.999x^3 + 121.870x^2 + 31.750x + 2.427. \tag{2}$$

By solving Eq. (2) equals zero, one can obtain that the sealing contact width L_s is 2.714 mm. Combining Eq. (1) and Eq. (2), it can be obtained that the average contact pressure P_{ca} equals 294.4 MPa.

2.2. Microchannels between Two Seal Surfaces. Test samples of the $7''$ casing PTC are shown in Figure 4. Three regions on the seal surfaces were randomly picked to be measured with Hitachi VS1800. The visual field in a single measurement is 1114.273 μm × 1114.770 μm. The topographies of the three measured regions after 10 times magnification of the objective lens are shown in Figure 5.

Seal surface topography typically consists of global-scale geometric features as well as local-scale roughness details [34]. We randomly picked two regions (with a fixed length and width of 236.65 μm and 109.30 μm) from the measured
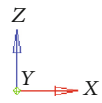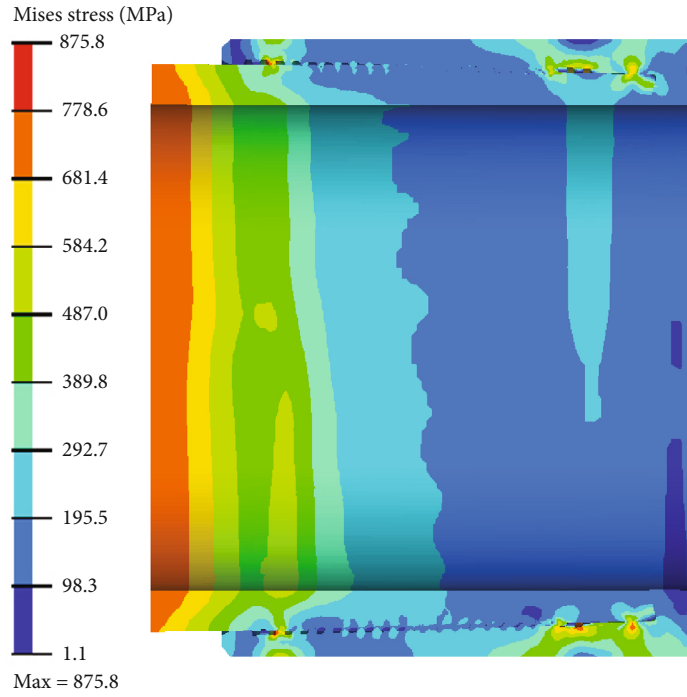
(a) von Mises stress
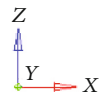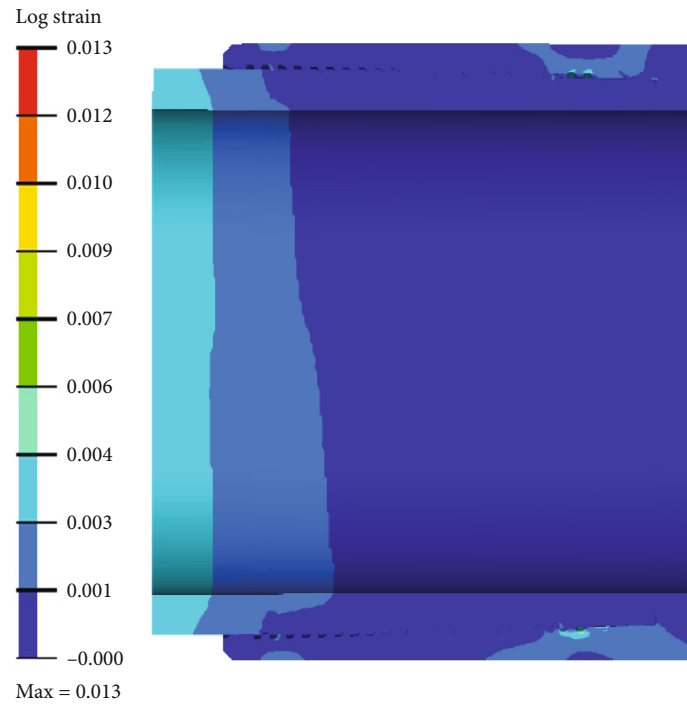
(b) Strain

FIGURE 2: Distributions of von Mises stress and strain of the 7″ casing PTC.
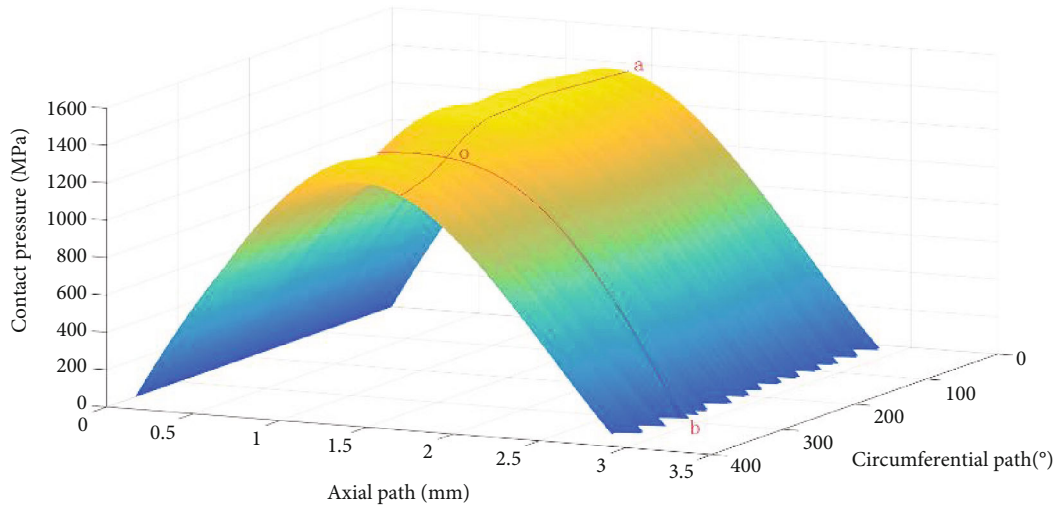
FIGURE 3: Distribution of contact pressure on the seal surface.

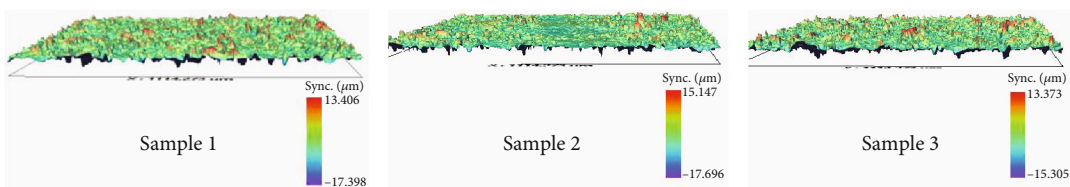FIGURE 4: Test samples of the $7''$ casing PTC.
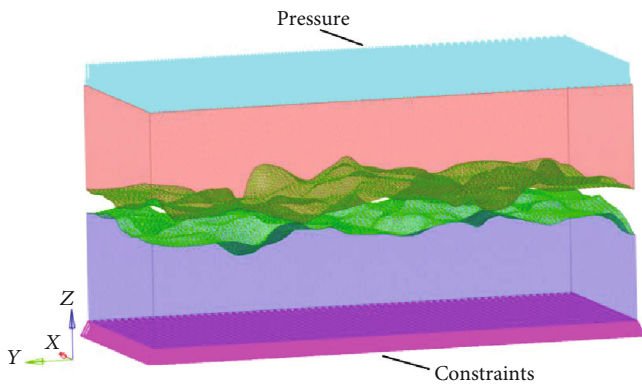

FIGURE 5: 3D topographies of the tested regions.

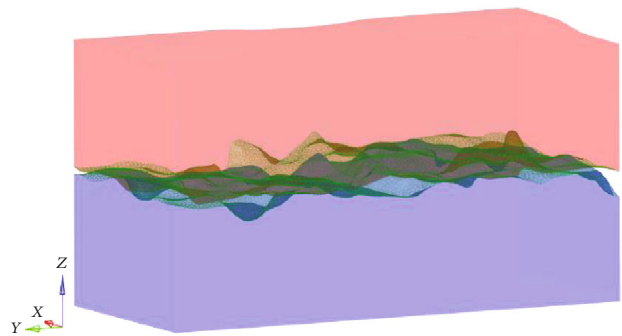FIGURE 6: Schematic of the microscopic sealing contact finite element model.

FIGURE 7: Deformed microscopic sealing contact finite element model and the microchannel between seal surfaces.

Contour plot
Displacement (Mag)
Analysis system

- 4.97E+00
- 4.42E+00
- 3.87E+00
- 3.32E+00
- 2.76E+00
- 2.21E+00
- 1.66E+00
- 1.11E+00
- 552.74E-3
- 0.00E+00

(a) Displacement

Contour plot
S-Stress components (Mises)
Simple average

- 1010.30
- 904.44
- 798.58
- 692.71
- 586.85
- 480.99
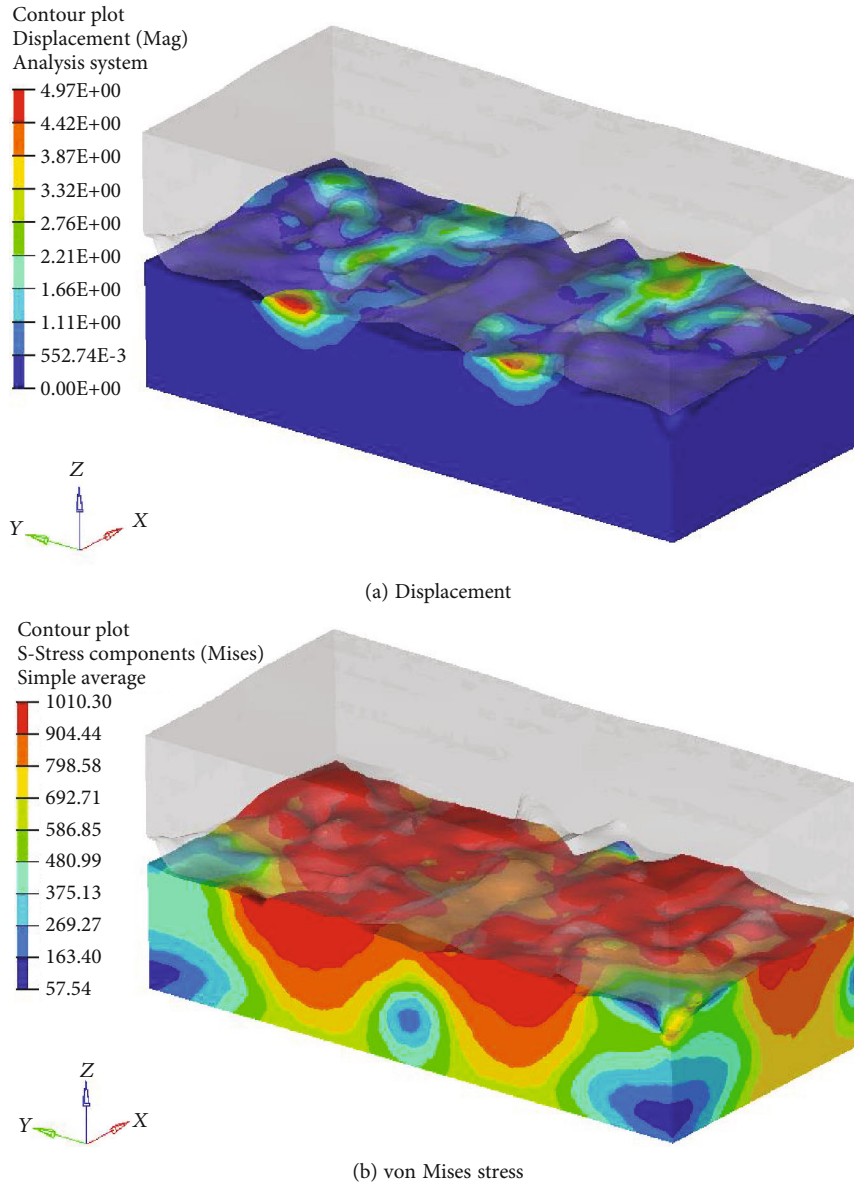- 375.13
- 269.27
- 163.40
- 57.54

(b) von Mises stress

Figure 8: Deformation and distribution characteristic of von Mises stress on the bottom seal surface.

topography of sample 1 to establish a microscopic sealing contact finite element model as shown in Figure 6. The red, blue, and green part represent the box, the pin, and the seal surfaces, respectively. Then, apply the average contact pressure of 294.4 MPa obtained in Section 2.1 to the upper surface of the sealing contact finite element model, and apply displacement constraints to the lower surface of the sealing contact finite element model, as shown in Figure 6. The topography features on the sealing surface are extruded under the effect of pressure, and a microchannel as shown in Figure 7 is obtained. The average clearance between the two seal surfaces is nearly 3.61 μm, and the volume of the microchannel is around 1.889×10^{-3} μm^3. Under the action of the average contact pressure, microstructures on the seal surfaces mutually squeeze each other. The corresponding deformation on the seal surfaces and the distribu-

tion characteristic of von Mises stress are shown in Figure 8. The maximum value of von Mises stress reaches 1010.3 MPa, indicating that plastic deformation occurs for certain regions on the seal surfaces.

3. Lattice Boltzmann Method

3.1. Multicomponent Shan-Chen Lattice Boltzmann Model. Due to its kinetic background, the LBM is extremely suitable for simulating flow problems of multiphase or multicomponent fluid at the microscopic scale [35, 36]. Comparing to conventional numerical methods, microscopic fluid-fluid or fluid-solid interactions can be easily incorporated in the framework of the LBM [25, 26, 37]. From the perspective of describing the interaction between fluid particles at the microscopic level, lattice Boltzmann (LB) multiphase models

can be roughly categorized into four categories: the color gradient model [38], the pseudopotential (Shan-Chen) model [39, 40], the free energy model [41], and the models based on the kinetic theory [42–46]. Fluid motion in the framework of the LBM is described by the evolution of particle density distribution functions. For the multicomponent Shan-Chen LB model, the evolution equations are given by [26].

$$f_i^\sigma(\mathbf{x} + \mathbf{c}_i \Delta t, t + \Delta t) - f_i^\sigma(\mathbf{x}, t) = -\frac{1}{\tau^\sigma}\left[f_i^\sigma(\mathbf{x}, t) - f_i^{\sigma,\mathrm{eq}}(\mathbf{x}, t)\right],$$
(3)

where $\mathbf{c}_i$ represents a set of discrete velocity, $f_i^\sigma(\mathbf{x}, t)$ is the σ th-component density distribution function in the ith direction of the discrete velocity set, $f_i^{\sigma,\mathrm{eq}}$ stands for the equilibrium density distribution function, and τ^σ is a relaxation time relates to the kinematic viscosity as $\nu^\sigma = (\tau^\sigma - (1/2))c_s^2 \Delta t$. The D3Q19 discrete velocity model proposed by Qian et al. [47] is used in this work, and the equilibrium distribution functions are given by

$$f_i^{\sigma,\mathrm{eq}} = \omega_i \rho^\sigma\left[1 + \frac{(\mathbf{c}_i \cdot \mathbf{u}^{\sigma,\mathrm{eq}})}{c_s^2} + \frac{(\mathbf{c}_i \cdot \mathbf{u}^{\sigma,\mathrm{eq}})^2}{2c_s^4} - \frac{(\mathbf{u}^{\sigma,\mathrm{eq}} \cdot \mathbf{u}^{\sigma,\mathrm{eq}})}{2c_s^2}\right],$$
(4)

where

$$\mathbf{c}_i = \begin{cases} (0,0,0)c, & i = 0, \\ (\pm 1,0,0)c, (0,\pm 1,0)c, (0,0,\pm 1)c, & i = 1, \cdots, 6, \\ (\pm 1,\pm 1,0)c, (\pm 1,0,\pm 1)c, (0,\pm 1,\pm 1)c, & i = 7, \cdots, 18, \end{cases}$$
(5)

$$\omega_i = \begin{cases} 1/3, & i = 0, \\ 1/18, & i = 1, \cdots, 6, \\ 1/36, & i = 7, \cdots, 18. \end{cases}$$
(6)

c_s is the lattice sound speed, $c_s^2 = (1/3)c^2$, and $c = \Delta x/\Delta t$ is the ratio of lattice spacing Δx and time step Δt.

The density and mass flux of the σth component of fluid are defined as

$$\rho^\sigma = \sum_i f_i^\sigma,$$
(7)

$$\rho^\sigma \mathbf{u}^\sigma = \sum_i \mathbf{c}_i f_i^\sigma.$$
(8)

For the multicomponent Shan-Chen LB model, the cohesive force acting on the σth component due to a different fluid component is defined as

$$\mathbf{F}_c^\sigma(\mathbf{x}) = -G_{\sigma\bar\sigma}\rho^\sigma(\mathbf{x}, t)\sum_i w_i \rho^{\bar\sigma}(\mathbf{x} + \mathbf{c}_i \Delta t, t)\mathbf{c}_i,$$
(9)

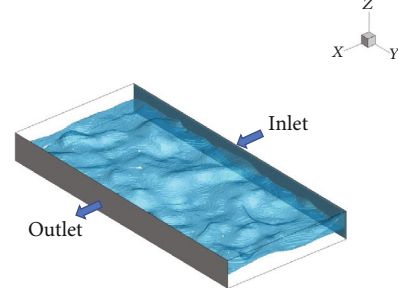where the subscripts σ and $\bar\sigma$ denote two different fluid com-

Figure 9: Schematic of the two component fluid system.

Table 3: Dimensional mapping between LB parameters and real dimensions.

Unit	Symbol	Dimensions	Mapping
Length	L	$[\mathrm{L}]$	$L_m = \delta x_{ph}/\delta x_{LB}$
Density	ρ	$[\mathrm{M}][\mathrm{L}]^{-3}$	$\rho_m = \rho_{ph}/\rho_{LB}$
Kinematic viscosity	ν	$[\mathrm{L}]^2[\mathrm{T}]^{-1}$	$\nu_m = \nu_{ph}/\nu_{LB}$
Time	t	$[\mathrm{T}]$	$t_m = L_m^2/\nu_m$
Mass	m	$[\mathrm{M}]$	$m_m = \rho_m L_m^3$
Velocity	U	$[\mathrm{L}][\mathrm{T}]^{-1}$	$U_m = L_m/t_m$
Force	F	$[\mathrm{M}][\mathrm{L}][\mathrm{T}]^{-2}$	$F_m = (m_m L_m)/t_m^2$
Pressure	P	$[\mathrm{M}][\mathrm{L}]^{-1}[\mathrm{T}]^{-2}$	$P_m = m_m/(L_m t_m^2)$

ponents and w_i represents a set of weight coefficients given by

$$w_i = \begin{cases} 1/18, & i = 1, \cdots, 6, \\ 1/36, & i = 7, \cdots, 18, \end{cases}$$
(10)

and $G_{\sigma\bar\sigma}$ is a parameter that controls the strength of the cohesive force. Similarly, the adhesive force acting on the σ th component due to a different solid component is given by

$$\mathbf{F}_{\mathrm{ads}}^\sigma(\mathbf{x}) = -G_{\mathrm{ads}}^\sigma \rho^\sigma(\mathbf{x}, t)\sum_i w_i s(\mathbf{x} + \mathbf{c}_i \Delta t, t)\mathbf{c}_i,$$
(11)

where G_{ads}^σ is a parameter that controls the strength of interaction between each fluid component and a solid wall and $s(\mathbf{x} + \mathbf{c}_i \Delta t, t)$ is an indicator function that equals to 1 or 0 for a solid wall or a fluid node, respectively.

The equilibrium velocity of the σth component is given by

$$\mathbf{u}^{\sigma,\mathrm{eq}} = \mathbf{u}' + \frac{\tau^\sigma(\mathbf{F}_c^\sigma + \mathbf{F}_{\mathrm{ads}}^\sigma)}{\rho^\sigma},$$
(12)

where $\mathbf{u}'$ is a common velocity given by the weighted average

$$\mathbf{u}' = \frac{\sum_\sigma(1/\tau^\sigma)\sum_i \mathbf{c}_i f_i^\sigma}{\sum_\sigma(1/\tau^\sigma)f_i^\sigma}.$$
(13)

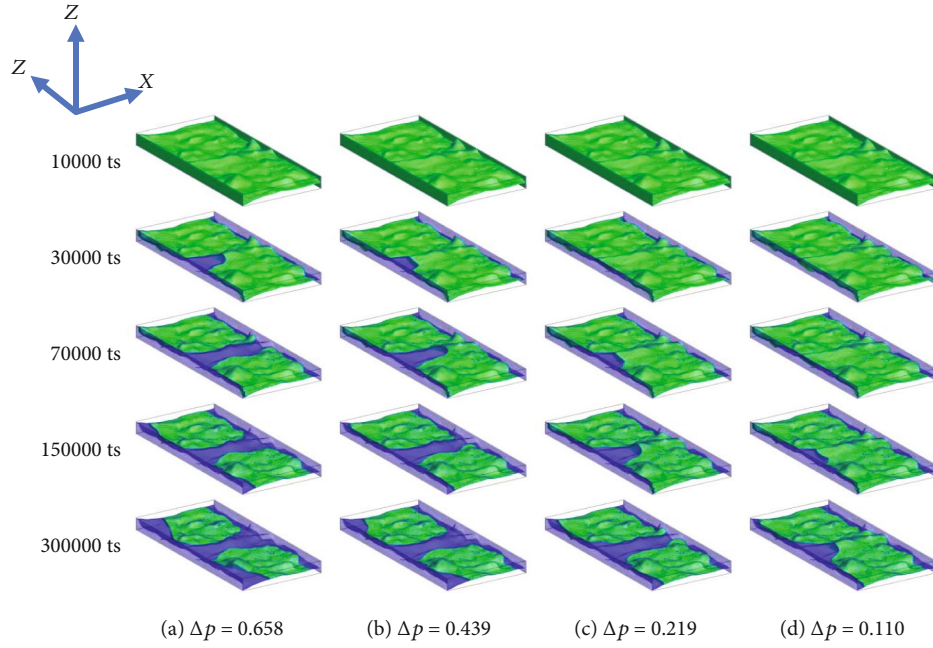(a) $\Delta p = 0.658$ (b) $\Delta p = 0.439$ (c) $\Delta p = 0.219$ (d) $\Delta p = 0.110$

FIGURE 10: Distributions of sealing compound inside the microchannels.
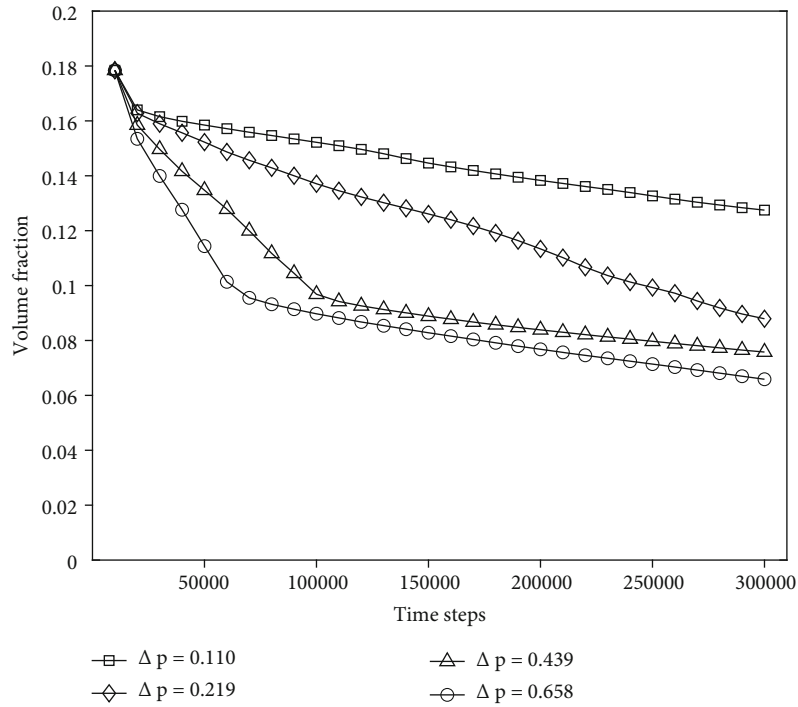

FIGURE 11: Time evolution of the volume fraction of sealing compound inside the microchannels.

Through the Chapman-Enskog analysis, the equation of state for the multicomponent Shan-Chen LB model in the continuum limit is

$$P(\mathbf{x}) = c_s^2 \sum_\sigma \rho^\sigma(\mathbf{x}) + 12c^2 G_{\sigma\bar\sigma} \rho^\sigma(\mathbf{x}) \rho^{\bar\sigma}(\mathbf{x}). \qquad (14)$$

The macroscopic density, velocity, and viscosity of the fluid mixture are given by

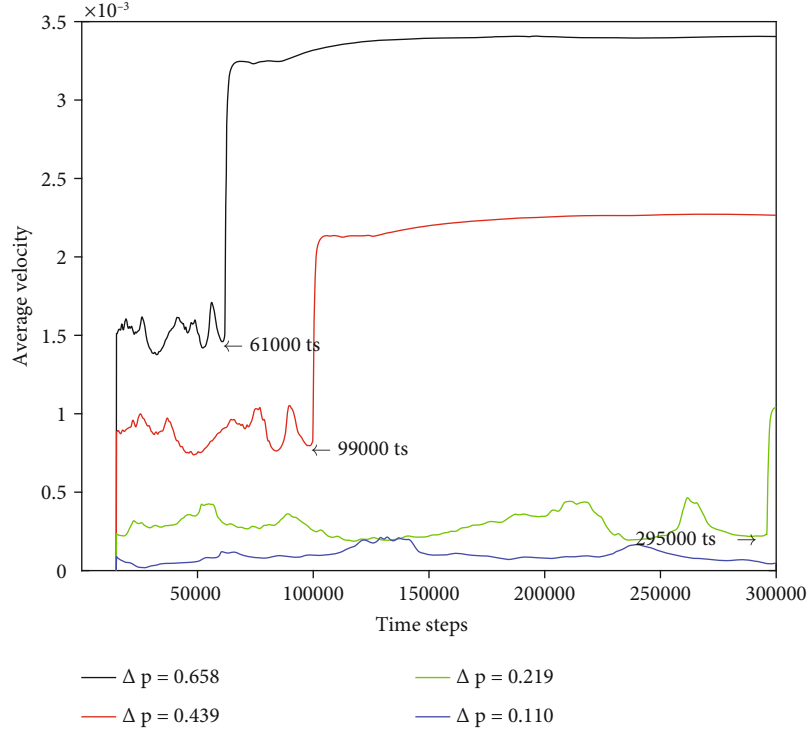$$\rho = \sum_\sigma \rho^\sigma, \qquad (15)$$

FIGURE 12: Time evolution of the average velocity of displacing fluid inside the microchannels.

TABLE 4: Contact angles according to $G_{ads,1}$.

$G_{ads,1}$	0.3	0.2	0.1	0	-0.2
θ	133.4°	117.3°	103.2°	90°	62.7°

$$\rho\mathbf{u} = \sum_\sigma \rho^\sigma \mathbf{u}^\sigma + \frac{1}{2}\sum_\sigma \mathbf{F}^\sigma_{total}, \qquad (16)$$

$$\nu = \frac{\sum_\sigma \rho^\sigma \tau^\sigma / \rho - 0.5}{3}\Delta t. \qquad (17)$$

3.2. Numerical Parameters and Boundary Conditions. The schematic of the two component fluid (displacing fluid and sealing compound) system is shown in Figure 9. The microchannel is assumed to be completely occupied by the sealing compound at the beginning of the simulation. The size of the computational domain is set to $222 \times 477 \times 47$, and the total number of time step in the simulation is set to 300000. The nonslip bounce back scheme is applied for the top, bottom, left, and right boundaries of the computational domain, while the pressure boundary condition proposed by Zou and He [48] is applied for the inlet and outlet. The viscosity ratio $M = \mu_1/\mu_2 = \nu_1\rho_1/\nu_2\rho_2$ in the current work equals 1.0.

The wetting condition for the wettability of the seal surfaces is given by

$$\cos\theta = \frac{G_{ads,2} - G_{ads,1}}{G_c((\rho_1 - \rho_2)/2)}, \qquad (18)$$

where $G_{ads,2} = -G_{ads,1}$ and θ stands for the contact angle.

Dimensional mapping presented in Table 3 is required for relating the LB parameters to real dimensions for practical use.

4. Results and Discussion

4.1. Effect of Pressure Gradient. At the beginning, the microchannels between the two seal surfaces are completely occupied by the sealing compound. The inlet and outlet pressure were kept consistent for 10000 time steps so that the multicomponent fluid system can relax towards equilibrium. After 10000 time steps, the outlet pressure was lowered. Driven by the pressure gradient due to the imbalance between the inlet and outlet pressure, the displacing fluid starts to penetrate the surrounding sealing compound. The distributions of sealing compound inside the microchannels at different time steps are shown in Figure 10. It is noticed that pressure gradient has a significant influence on the distribution of sealing compound. For the systems with larger pressure gradient (Figures 10(a)–10(c)), the displacing fluid tends to break through the surrounding sealing compound more rapidly and forms a dominant flow channel, while it may even fails to break through the sealing compound for the system with the lowest pressure gradient (Figure 10(d)). For the system with the highest pressure gradient (Figure 10(a)), the displacing fluid has broken through the surrounding sealing compound before 70000 time steps. For the system with $\Delta p = 0.439$, a dominant flow channel has been formed at 150,000 time steps. For the system with $\Delta p = 0.219$, the displacing fluid just finishes breaking through the sealing compound and the dominant flow
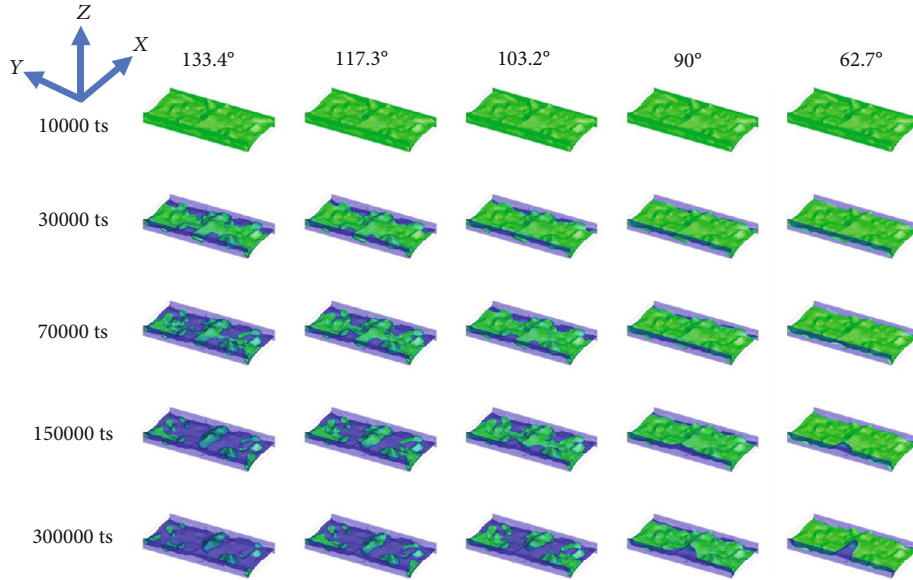
FIGURE 13: Snapshots of distributions of sealing compound inside the microchannel with different wettability.
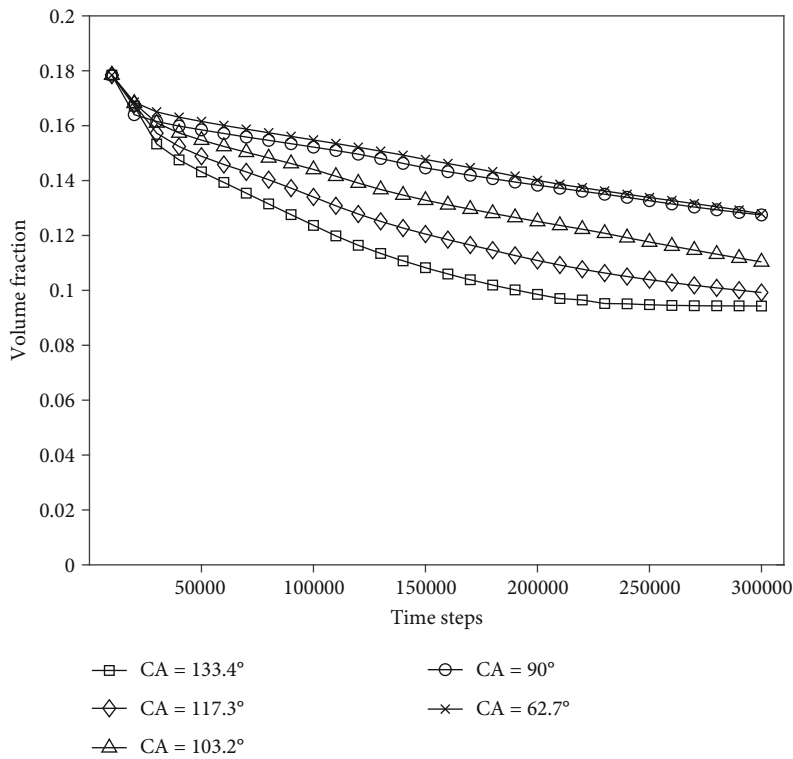

FIGURE 14: Time evolution of the volume fraction of sealing compound inside the microchannels with various wettability.

channel are not yet fully developed. For the system with the lowest pressure gradient (Figure 10(d)), more time steps may be required.

To understand the flow characteristics inside the microchannels, the variation of the volume fraction of sealing compound and the average velocity of displacing fluid are shown in Figures 11 and 12. As time elapses, the volume fraction of sealing compound gradually decreases. Larger

values of pressure gradient eventually lead to a lower volume fraction. Meanwhile, for the systems with larger pressure gradient ($\Delta p = 0.658$, $\Delta p = 0.439$), whether the displacing fluid has broken through the surrounding sealing compound can be directly acknowledged from the slope of the data curve. The volume fraction of sealing compound decreases more rapidly at the break-through stage. Similarly, this characteristic can also be observed from Figure 12. For the

systems with larger pressure gradient, the average velocity of displacing fluid during the leaking stage is much higher than that before the break-through. To be specific, for the systems with $\Delta p = 0.658$, $\Delta p = 0.439$, and $\Delta p = 0.219$, the break-through time steps are around 61000, 99000, and 295000, respectively. Compared with the leaking stage, the average velocity is not that stable during the break-through stage.

4.2. Effect of Wettability. Similar to the above cases, the microchannel between the seal surfaces is completely occupied by the sealing compound at the beginning. The inlet pressure and outlet pressure were kept consistent for 10000 time steps. After 10000 time steps, the outlet pressure was lowered. The pressure difference was fixed at $\Delta p = 0.110$ in these cases. For the parameters in this work, the corresponding wettability of the seal surfaces according to $G_{ads,1}$ are listed in Table 4. When $G_{ads,1} > 0$, the microchannel is wetting for the displacing fluid and nonwetting for the sealing compound and vice versa. Numerical instability was observed when $G_{ads,1} < -0.2$, and the results were not included. The distributions of sealing compound inside the microchannels with various wettability are shown in Figure 13. It can be noticed that wettability has huge impact on the distribution of sealing compound. The variation of the volume fraction of sealing compound as time elapses is shown in Figure 14. A smaller volume fraction can be obtained if the seal surfaces are nonwetting for the sealing compound (wetting for the displacing fluid), while a finger forwarding phenomena was noticed if the seal surfaces were wetting for the sealing compound (nonwetting for the displacing fluid). No break-through was observed for the fixed pressure difference if the seal surfaces were wetting for the sealing compound.

5. Conclusions

This study obtained a microchannel between the seal surfaces of casing connection under complex loads combining 3D elastoplastic FEA and the topographies of seal surfaces. The flow behavior of the microchannel was analyzed with the LBM. It is expected to provide some new insights for studying the seal failure of casing connections. The major findings are summarized below:

(1) The contact pressure on the seal surfaces of casing threaded connection under complex loads is uneven in both circumferential and axial directions. According to the seal contact energy theory, an average contact pressure can be obtained as the external load being applied on the microscopic sealing contact finite element model

(2) A microscopic sealing contact finite element model based on the topographies of the seal surfaces scanned by the optical interference measuring system was established. After applying the average contact pressure, the deformed seal surfaces under complex loads can be obtained. For the topography and loading condition in this work, the average

clearance of the microchannel between the deformed seal surfaces is nearly $3.61\,\mu$m, and the volume of the microchannel equals $1.889 \times 10^{-3}\,\mu$m^3

(3) The effect of pressure gradient on the flow behavior of a multicomponent system inside the microchannel between the seal surfaces was simulated by the LBM. The volume fraction of sealing compound inside the microchannels decreases when the pressure gradient increases. For the systems with larger pressure gradient, a break-through stage and a leaking stage can be observed. The average velocity of displacing fluid slightly fluctuates during the break-through stage. For the leaking stage, the average velocity of displacing fluid increases immediately once the dominant flow channel is formed and then tends to stabilize at a higher level

(4) Break-throughs were captured from the simulation for the systems with $\Delta p = 0.658$, $\Delta p = 0.439$, and $\Delta p = 0.219$. And the break-through time steps are around 61000, 99000, and 295000, respectively. Displacing fluid was not able to break through the surrounding sealing compound for the system with the lowest pressure gradient. The average velocity of displacing fluid after the break-through actually reflects the leakage rate of the seal at the microscopic level; a further detailed analysis will be presented in future work

(5) The effect of wettability on the flow behavior inside the microchannel between the seal surfaces of casing connection for a fixed pressure difference was simulated by the LBM. It has huge impact on the distribution of sealing compound. No break-through was observed for the fixed pressure difference

Data Availability

The data used to support the findings of this study have not been made available because the author has no permission to publish.

Conflicts of Interest

The authors declare that there is no conflict of interest regarding the publication of this paper.

Authors' Contributions

Feng Ye is responsible for the methodology, LBM simulation, formal analysis, and writing—original draft; Feng Chen for the conceptualization, methodology, finite element analysis, and writing—original draft; Wenchang Wang for the investigation, formal analysis, and writing—review and editing; Renliang Zhang for the methodology, LBM simulation, and formal analysis; Xing Zhou for the investigation and experiment; Ken Qin for the investigation and experiment; and Qinfeng Di for the conceptualization, formal analysis, resources, and writing—review and editing.

Acknowledgments

References

[1] Y. Feng, L. Han, F. Zhang, Z. Bai, and W. Liu, "Research progress and prospect of oil and gas well tubing string integrity technology," *Natural Gas Industry*, vol. 34, no. 11, pp. 73–81, 2014.

[2] F. Dalla Vecchia, V. H. J. M. dos Santos, M. K. Schütz et al., "Wellbore integrity in a saline aquifer: experimental steel-cement interface degradation under supercritical CO_2 conditions representative of Brazil's Parana basin," *International Journal of Greenhouse Gas Control*, vol. 98, article 103077, 2020.

[3] E. Khodami, A. Ramezanzadeh, and M. Noroozi, "Numerical modeling of oil well integrity with a particular view to cement (case study: Maroon Oilfield in southwest of Iran)," *Journal of Petroleum Science and Engineering*, vol. 196, p. 107991, 2021.

[4] J. Li, S. Ding, L. Han, and Q. Tao, "Research progress on failure mechanism and control methods of wellbore integrity during multi-stage fracturing of shale gas," *Petroleum Tubular Goods & Instruments*, vol. 6, no. 4, pp. 10–15, 2020.

[5] L. Sun, Z. Chen, H. Huo, L. Zhang, W. Wang, and H. Zhao, "Collapse risk analysis of casing string under the action of non-uniform crustal stress," *Technology Supervision in Petroleum Industry Journal Agency*, vol. 36, no. 4, pp. 37–39, 2020.

[6] F. Yin and D. Gao, "Mechanical analysis and design of casing in directional well under in-situ stresses," *Journal of Natural Gas Science and Engineering*, vol. 20, pp. 285–291, 2014.

[7] H. Zhang, R. Shen, G. Yuan, Z. Ba, and Y. Hu, "Cement sheath integrity analysis of underground gas storage well based on elastoplastic theory," *Journal of Petroleum Science and Engineering*, vol. 159, pp. 818–829, 2017.

[8] K. Hamilton, B. Wagg, and T. Roth, "Using ultrasonic techniques to accurately examine seal-surface-contact stress in premium connections," *SPE Drilling and Completion*, vol. 24, no. 4, pp. 696–704, 2009.

[9] B. E. Schwind, "Equations for leak resistance of API 8-round connectors in tension," *SPE Drilling Engineering*, vol. 5, no. 1, pp. 63–70, 1990.

[10] W. Gong, "Relation between sealing ability and tolerance range of casing threads," *China Petroleum Machinery*, vol. 4, pp. 30–34, 1996.

[11] Z. Xu, X. Yan, and X. Yang, "Integrity evaluation method for non-API casing connections," *Gongcheng Lixue/Engineering Mechanics*, vol. 33, no. 2, pp. 188–199, 2016.

[12] H. Xu, B. Yang, T. Shi, and Z. Zhang, "Analysis of factors influencing hermetic seal performance with a spherical-conical surface and special screw threads," *Xinan Shiyou Daxue Xuebao/Journal of Southwest Petroleum University*, vol. 39, no. 6, pp. 162–166, 2017.

[13] T. Mimaki, M. Ogasawara, and Y. Yazaki, "Criterion for gas seal tightness of premium connection of oil country tubular goods," *Journal of High Pressure Institute of Japan*, vol. 35, no. 2, pp. 65–78, 1997.

[14] M. Ogasawara, F. Koyama, K. Maruyama et al., "Development of nippon steel premium connections," *Nippon Steel Technical Report*, vol. 38, pp. 10–17, 1988.

[15] C. Marie, D. Lasseux, H. Zahouani, and P. Sainsot, "An integrated approach to characterize liquid leakage through metal contact seal," *European Journal of Mechanical and Environmental Engineering*, vol. 48, no. 2, pp. 81–86, 2003.

[16] G. R. Murtagian, V. Fanelli, J. A. Villasante, D. H. Johnson, and H. A. Ernst, "Sealability of stationary metal-to-metal seals," *Journal of Tribology*, vol. 126, no. 3, pp. 591–596, 2004.

[17] J. Xie and S. Hassanein, *In Reliability-Based Design and Assessment (RBDA) Method for Thermal Wells*, World Heavy Oil Congress, Aberdeen, Britain, 2012.

[18] J. Xie, "In numerical evaluation of tubular connections for HPHT applications," in *5th Baosteel Biennial Academic Conference*, Shanghai, China, 2013.

[19] J. Wang, Y. Feng, K. Lin, C. Qin, and Y. Song, "Comparison analysis of premium connection's seal structure," *Journal of China University of Petroleum (Edition of Natural Science)*, vol. 34, no. 5, pp. 126–130, 2010.

[20] F. Chen, Q. Di, N. Li, C. Wang, W. Wang, and M. Wang, "Determination of operating load limits for rotary shouldered connections with three-dimensional finite element analysis," *Journal of Petroleum Science and Engineering*, vol. 133, pp. 622–632, 2015.

[21] Q. Di, F. Chen, W. Wang et al., "Three-dimensional mechanical analysis of the double-shouldered tool joint," *Acta Petrolei Sinica*, vol. 33, no. 5, pp. 871–877, 2012.

[22] Y. Dou, L. Ma, M. Li, and Y. Yu, "Finite element analysis of premium connection with less or over make-up torque," *Oil Field Equipment*, vol. 45, no. 4, pp. 52–56, 2016.

[23] A. R. Shahani and S. M. H. Sharifi, "Contact stress analysis and calculation of stress concentration factors at the tool joint of a drill pipe," *Materials and Design*, vol. 30, no. 9, pp. 3615–3621, 2009.

[24] X. Zhu, Z. Zhang, X. Chang, and L. Li, "Three-dimensional mechanical behavior of worn casing connecting thread in complex structural well," *Acta Petrolei Sinica*, vol. 36, no. 6, pp. 748–753, 2015.

[25] H. Huang, M. C. Sukop, and X. Y. Lu, *Multiphase Lattice Boltzmann Methods: Theory and Application*, Wiley-Blackwell, 2015.

[26] M. C. Sukop and D. T. Thorne, *Lattice Boltzmann Modeling: an Introduction for Geoscientists and Engineers*, Springer, 2006.

[27] J. Li, M. T. Ho, L. Wu, and Y. Zhang, "On the unintentional rarefaction effect in LBM modeling of intrinsic permeability," *Advances in Geo-Energy Research*, vol. 2, no. 4, pp. 404–409, 2018.

[28] J. Li and D. Brown, "Upscaled lattice Boltzmann method for simulations of flows in heterogeneous porous media," *Geofluids*, vol. 2017, Article ID 1740693, 12 pages, 2017.

[29] Z. Peng, S. Liu, S. Tang, Y. Zhao, and Y. Li, "Multicomponent lattice Boltzmann simulations of gas transport in a coal reservoir with dynamic adsorption," *Geofluids*, vol. 2018, Article ID 5169010, 2018.

[30] G. Zhang, B. Liu, A. Xu, Y. Shan, and Y. Li, "Morphology effect of surface structures on microchannel flow using lattice Boltzmann method," *Geofluids*, vol. 2019, Article ID 3475872, 2019.

[31] G. Xu, Y. Du, J. Zhou, Y. Tian, and X. Huang, "Numerical analysis of gas tightness of seals in pSOFCs based on lattice

Boltzmann method simulation," *International Journal of Hydrogen Energy*, vol. 44, no. 38, pp. 21136–21147, 2019.

[32] API, *SPEC 5B: Specification for Threading, Gauging and Thread Inspection of Casing, Tubing, and Line Pipe Threads*, American Petroleum Institute, 15th edition, 2008.

[33] H. Xu, *Study on Joint Strength and Sealing Theory for Casing and Tubing Premium Connections*, Southwest Petroleum University, 2015.

[34] F. Perez-Rafols, R. Larsson, S. Lundstrom, P. Wall, and A. Almqvist, "A Stochastic Two-Scale Model for Pressure-Driven Flow Between Rough Surfaces," *Proceedings of the Royal Society a-Mathematical Physical and Engineering Sciences*, vol. 472, no. 2190, 2016.

[35] Y. Cao, M. Tang, Q. Zhang, J. Tang, and S. Lu, "Dynamic Capillary Pressure Analysis of Tight Sandstone Based on Digital Rock Model," *Capillarity*, vol. 3, no. 2, pp. 28–35, 2020.

[36] G. Zhang, Y. Zhang, A. Xu, and Y. Li, "Microflow effects on the hydraulic aperture of single rough fractures," *Advances in Geo-Energy Research*, vol. 3, no. 1, pp. 104–114, 2019.

[37] F. Ye, Q. Di, W. Wang, F. Chen, H. Chen, and S. Hua, "Comparative study of two lattice Boltzmann multiphase models for simulating wetting phenomena: implementing static contact angles based on the geometric formulation," *Applied Mathematics and Mechanics (English Edition)*, vol. 39, no. 4, pp. 513–528, 2018.

[38] A. K. Gunstensen, D. H. Rothman, S. Zaleski, and G. Zanetti, "Lattice Boltzmann model of immiscible fluids," *Physical Review A*, vol. 43, no. 8, pp. 4320–4327, 1991.

[39] X. Shan and H. Chen, "Lattice Boltzmann model for simulating flows with multiple phases and components," *Physical Review E*, vol. 47, no. 3, pp. 1815–1819, 1993.

[40] X. Shan and H. Chen, "Simulation of nonideal gases and liquid-gas phase transitions by the lattice Boltzmann equation," *Physical Review E*, vol. 49, no. 4, pp. 2941–2948, 1994.

[41] M. R. Swift, W. R. Osborn, and J. M. Yeomans, "Lattice Boltzmann simulation of nonideal fluids," *Physical Review Letters*, vol. 75, no. 5, pp. 830–833, 1995.

[42] Z. Guo and T. S. Zhao, "Discrete velocity and lattice Boltzmann models for binary mixtures of nonideal fluids," *Physical Review E*, vol. 68, no. 3, article 035302, 2003.

[43] X. He, S. Chen, and R. Zhang, "A lattice Boltzmann scheme for incompressible multiphase flow and its application in simulation of Rayleigh-Taylor instability," *Journal of Computational Physics*, vol. 152, no. 2, pp. 642–663, 1999.

[44] X. He, X. Shan, and G. D. Doolen, "Discrete Boltzmann equation model for nonideal gases," *Physical Review E*, vol. 57, no. 1, pp. R13–R16, 1998.

[45] L. S. Luo, "Unified theory of lattice Boltzmann models for nonideal gases," *Physical Review Letters*, vol. 81, no. 8, pp. 1618–1621, 1998.

[46] H. Wang, X. Yuan, H. Liang, Z. Chai, and B. Shi, "A brief review of the phase-field-based lattice Boltzmann method for multiphase flows," *Capillarity*, vol. 2, no. 3, pp. 33–52, 2019.

[47] Y. H. Qian, D. D'Humières, and P. Lallemand, "Lattice BGK models for Navier-Stokes equation," *Europhysics Letters (EPL)*, vol. 17, no. 6, pp. 479–484, 1992.

[48] Q. Zou and X. He, "On pressure and velocity boundary conditions for the lattice Boltzmann BGK model," *Physics of Fluids*, vol. 9, no. 6, pp. 1591–1598, 1997.